

**Taming Polysulfides in Sulfur-based Batteries via
Electrolyte-soluble Thiomolybdate Additives**

Journal:	<i>Journal of Materials Chemistry A</i>
Manuscript ID	TA-ART-05-2022-003893.R1
Article Type:	Paper
Date Submitted by the Author:	07-Jul-2022
Complete List of Authors:	Yaghoobnejad Asl, Hooman; The University of Texas at Austin Bhargav, Amruth; The University of Texas at Austin Manthiram, Arumugam; The University of Texas at Austin, Materials Science and Engineering

Taming Polysulfides in Sulfur-based Batteries via Electrolyte-soluble Thiomolybdate

Additives

Hooman Yaghoobnejad Asl¹, Amruth Bhargav¹, Arumugam Manthiram^{1,*}

¹ Materials Science and Engineering Program and Texas Materials Institute, University of Texas at Austin, Austin, TX 78712, USA.

Abstract. The promise of secondary sulfur-based batteries as a sustainable and low-cost alternative to electrochemical energy storage has been long held back by the polysulfide shuttle problem. Herein, we demonstrate the utilization of electrolyte-soluble additives based on (oxo)thiomolybdate as a tool to mitigate the effect of the polysulfide shuttle in secondary sulfur-based batteries. Through a variety of techniques, it is shown that the Mo-containing anionic additives undergo spontaneous nucleophilic reactions with the highly soluble, long-chain polysulfides via a neutral S-atom transfer process, yielding higher S/Mo ratio complexes along with short-chain polysulfides. More importantly, it is shown how the O/S atomic substitution on the molybdenum center can induce enzymatic-level enhancement in the above reaction rate by lowering the homolytic S-S bond cleavage energy. Lastly, through anode-level inspections, it was realized that the dendritic electroplating of Li was suppressed considerably in the system with oxo/thiomolybdate, thereby reducing the cell impedance and overpotential, leading to significantly improved cycle-life. The positive influence of the increased polysulfide uptake reaction kinetics is evidenced by stable cycle-life and a low capacity-fade rate of 0.1 % per cycle in Li-S cells with a high sulfur loading and lean electrolyte compositions.

INTRODUCTION

Secondary (*i.e.*, rechargeable) batteries based on sulfur cathodes have been amongst the highly sought after solutions for widespread electrification and renewable energy utilization and a major enabler of the transition from fossil fuels to clean energy.¹⁻⁶ The interest in S cathode emanates from its high natural abundance, low toxicity, and the high energy-density associated with S/S²⁻ reduction reaction, giving rise to a theoretical gravimetric energy density of 2.5 kWh kg⁻¹ at the electrode level in Li-S cells.^{1,7,8} Due to the insulating nature of both the endmembers S and Li₂S, a direct solid-solid electrochemical conversion is not a naturally favored reaction pathway. Instead, the reduction of S follows through stepwise reactions, starting from reductive S₈ ring-opening and formation of electrolyte-soluble long-chain polysulfides (PS) Li₂S_x ($x \leq 8$), to further gradual S reduction and PS chain cleavage, ultimately resulting in Li₂S formation.¹ While the solution-mediated PS chemistry is instrumental to the operation of secondary batteries, it is also the source of cycling instability, self-discharge, and capacity degradation by the notorious PS shuttle problem. Briefly, the dissolved PS diffuse freely to the anode, get reduced fully or partially on the surface of the reactive lithium-metal anode, thereby creating an internal loop that extensively consumes the S-cathode, Li-anode, along with the electrolyte.^{9,10} Sodium-sulfur (Na-S) batteries with a high energy density of 1.3 kWh kg⁻¹ are another emerging and promising technology, with sustainability and further reduction in cost. Sharing a similar chemistry with the lithium counterpart, the same challenges listed above beleaguer the development of Na-S technology.

The key to the development of both Li-S and Na-S chemistries lies in deterring the shuttling of PS. Historically, the PS shuttle problem was addressed through blending-in solid ingredients either into the cathode composite or on the separator that could bind the anionic PS

species through a variety of atomic-level forces, and hence restraining the mobility of the PS. These interactions can vary from low-energy Van der Waals forces between the polarizable electron-density of the bridging S atoms in the PS with that of the π -bonding orbitals of carbonaceous materials, to the stronger Lewis acid-base interactions between the anionic terminal S atoms of the PS and the cationic metals,³ to even the more energetic redox pathways.¹¹ In general, the heterogeneous interaction between the liquid electrolyte-soluble PS and a solid host suffers from two major limitations: (i) incorporation of the solid host into cathode composite often requires complicated and multi-step processes,¹² and (ii) due to the heterogeneity of the interaction, a high surface-area and extreme down-sizing of the PS host is needed.¹³ The high porosity and surface area of the PS host necessitate the utilization of larger amounts of electrolyte due to soaking, thus significantly diminishing the practical energy density of the cell.¹⁴ Therefore, until now the main strategy in tackling the polysulfide shuttle challenge was centered over the use of heterogeneous (*i.e.*, solid) additive. Herein, we report for the first time the synergistic effect of homogeneous (*i.e.*, electrolyte-soluble) Mo-containing additives via an admixture of oxo-thio ligands to tune the rate of additive-polysulfide reaction.

In general, an ideal remedy to the PS shuttle problem involves the utilization of additives that require a minimal amount of pre-processing, can be easily introduced into the cell, and can dissolve into the electrolyte to initiate homogeneous solution-phase interactions with the soluble PS species, thereby suppressing or eliminating the shuttling problem. Pursuant to these criteria, our group aimed at exploring the interaction of transition-metal sulfides with PS species and their effects on the regulation of the PS shuttle problem in secondary S-based batteries. One notable example of this category is Mo-based thio-complexes and compounds, which are known for their catalytic role in various reactions. Due to adopting various oxidation states up to +6 and diverse

coordination environments, Mo is an interesting atom from a chemical point of view. For example, nature uses Mo in molybdo-enzymes as an active-site for nitrogen fixation in N_2 to NH_4^+ reduction in a variety of nitrogenase enzymes,^{15,16} or in dimethyl sulfoxide (DMSO) reductase, which reduces the sulfur atom in DMSO to dimethyl sulfide (DMS) and water using electrons and protons¹⁷. Furthermore, Mo-based compounds are used extensively as man-made heterogeneous catalysts for hydrodesulfurization of heavy crude oil as well as for homogeneous electrocatalysts in hydrogen evolution and water splitting reactions.^{18,19} Such examples demonstrate the high potentials of the utilization of homogeneous reactions of Mo-based compounds in niche applications, such as secondary S-based batteries, an area that has been less touched by battery scientists so far.

In this work, we are using two simple Mo-based complexes, $MoO_2S_2^{2-}$ and MoS_4^{2-} , as homogeneous (*i.e.*, electrolyte-soluble) additives in Li-S cells to demonstrate their effect on suppressing the PS effect and stabilizing the cell operation. The investigation details to understand the reaction mechanisms and kinetics by which PS species interact with the additives. Importantly, it is observed that an oxo/thio ligand admixture as in $MoO_2S_2^{2-}$ imparts catalytic-level increase in the PS uptake reaction compared to the MoS_4^{2-} counterpart, an observation assigned to the relative ease of formation of diradicals in the oxo-thio molybdate complex. Thus, the faster PS sequestration kinetics of $MoO_2S_2^{2-}$ leads to a superior regulation of the shuttle problem compared to the MoS_4^{2-} analog. Also, in combination with the liquid-phase investigations, it was observed that the dendritic electrodeposition of Li is considerably suppressed in cells with additives, with a relative efficiency of $MoO_2S_2^{2-} > MoS_4^{2-} \gg$ blank. The excessive dendritic electrodeposition of Li – which is blamed on the polysulfide reaction on the surface of Li anode - is the main reason for the formation of dead lithium, increased electrolyte-

anode side reactions and formation of a thick SEI, and fast cell failure through catastrophic internal anode-cathode shorting. The above synergistic effects of fast polysulfide shuttle regulation via incorporation of $\text{MoO}_2\text{S}_2^{2-}$ additives is well demonstrated in “fail-fast” cells, *i.e.*, cells with high mass-loadings of elemental sulfur cathode and limited amounts of electrolyte engineered to expedite the ultimate catastrophic failure under demanding conditions.

The concept of using electrolyte-soluble additives to mitigate the impact of polysulfide shuttle is a new area in metal-sulfur batteries. These approaches tend to simplify the process of electrode and cell fabrication. This is because the additives are introduced into the cell as solubilized species in the electrolyte or are physically mixed with the cathode and allowed to dissolve in the electrolyte during the formation cycles. This is in contrast with the common methods of cathode engineering through nanochemistry, by which polysulfide species are retained at the surface of the cathode. An important aspect in the chemistry of electrolyte-soluble additives is (i) the reaction mechanism of reactive polysulfide species with the additive molecules and (ii) understanding the secondary effects of this reaction on the morphology of the deposited lithium on the anode surface. For the former, the reaction kinetics play an important role in the confinement of the polysulfide species, while the latter determines the overall rate of cell failure through irreversible Li inventory consumption or possible catastrophic internal short circuits. In this work, we demonstrate that through heteroatomic O/S substitution on the $\text{MoS}_2\text{X}_2^{2-}$ electrolyte-soluble additives (X: S/O), one can increase considerably the reaction rate between $\text{MoS}_2\text{X}_2^{2-}$ and S_x^{2-} ($x \leq 8$), thereby improving the efficiency of confining the reactive polysulfides within the electrolyte. Furthermore, it is shown that the more reactive $\text{MoO}_2\text{S}_2^{2-}$ species react at the surface of Li anode to provide a stable MoS_2 -rich SEI, giving rise to improved electrodeposited Li metal morphologies.

EXPERIMENTAL SECTION

Syntheses. $(\text{NH}_4)_2\text{MoO}_2\text{S}_2$ was obtained as a pure, orange, crystalline solid by mixing 1.2359 g (1 mmol) of $(\text{NH}_4)_6\text{Mo}_7\text{O}_{24}\cdot 4\text{H}_2\text{O}$ (Sigma-Aldrich, 99.98% purity) in 30% ammonia solution (Fisher Chemical, ACS Plus grade) with 15 mL of $(\text{NH}_4)_2\text{S}$ solution (Fisher Chemical, 20% in H_2O). Upon mixing, the solution turned orange immediately, followed by nucleation and growth of $(\text{NH}_4)_2\text{MoO}_2\text{S}_2$ within seconds. The crystals were immediately separated from the mother liquor by centrifugation, washed sequentially with aqueous ammonia solution, ethanol, and acetone, and finally dried at 50 °C under vacuum; the purity of the product was analyzed with powder X-ray diffraction.

$((\text{CH}_3)_4\text{N})_2[(\eta\text{-S}_2)\text{Mo}_2\text{O}_2(\mu\text{-S})_2(\eta\text{-S}_4)]\cdot\text{CH}_3\text{CN}$ was synthesized under an inert environment by first dissolving 0.0912 g (0.4 mmol) of $(\text{NH}_4)_2\text{MoO}_2\text{S}_2$ in 3 mL of dry N,N-dimethyl formamide (DMF) heated to 85 °C, to which 0.1030 g (0.4 mmol as S_8) of S was added. The homogeneous solution was kept at this temperature for 2 h, and 0.1100 g $(\text{CH}_3)_4\text{NCl}$ (1.0 mmol) was added and the mixture was removed from the heat. The mixture was left undisturbed for 48 h, then the solution was separated from the excess $(\text{CH}_3)_4\text{NCl}$ by decantation, and DMF was removed by evaporation under vacuum at 80 °C. The dark-brown solid was dissolved in 3 mL of anhydrous acetonitrile, and the solvent was evaporated slowly at room temperature over the course of 3 days. Large, brittle, plate-like orange crystals of the title compound were obtained, which were used for structure solution via single-crystal X-ray diffraction.

Characterization. Powder X-ray diffraction (PXRD) analysis was carried out with a Rigaku Miniflex 600 diffractometer equipped with a Cu $K\alpha$ source.

Single-crystal X-ray diffraction (SC-XRD) analysis was carried out with an Agilent SuperNova 4-axes diffractometer. The crystalline sample was dispersed in heavy mineral oil, and an appropriate crystal was mounted directly onto a nylon loop and transferred to the goniometer head. In total, X diffraction frames were acquired by scanning the angular ranges of ω , ϕ , κ , and 2θ axes at 100 K under N_2 purge, for which the intensities were corrected for the dark current. The positions of heavy Mo and S atoms within the asymmetric unit were located using the direct method, which was further refined with SHELX 2003. Furthermore, positions of the remaining O, N, and C atoms were found and refined anisotropically from the Fourier difference map search. Finally, the H atoms were located from the Fourier map search or assigned intuitively, and these positions were refined isotropically in order to complete the structure. X-ray photoelectron spectroscopy (XPS) was performed on a Kratos AXIS Ultra DLD spectrometer with monochromatic Al $K\alpha$ radiation. Data were analyzed using the CASA XPS software wherein the adventitious carbon peak set at 284.8 eV was used to calibrate the spectra. Tougaard background was used along with Gaussian/Lorentzian peaks for peak fitting. SEM images were obtained on a FEI Quanta 650 SEM operated at 15 kV.

Chronoamperometry tests were conducted in order to obtain an insight into the reaction kinetics of the PS with the additives under conditions similar to that in a Li-S cell. These tests were run under Ar in glass test tube cells loaded with a Teflon-coated magnet bar, fitted with a rubber septum through which two inert Monel wires were fed that are acting as symmetric electrodes. In each test, the reaction mixture containing 0.1 mmol of the PS species (average composition as Li_2S_8) and 0.14 mmol of $(NH_4)_2MoS_4$ or $(NH_4)_2MoO_2S_2$ additives in 2 mL of 1:1 v/v mixture of 1,3-dioxolane and 1,2-dimethoxyethane (DOL-DME) was charged into the glass cells and capped, and a potential of 1.0 V was applied for more than 10 h from a VoltaLab

PST050 potentiostat to the electrodes while the mixture is under constant stirring (Figure S3). The applied potential is large enough for the interconversion of PS species and yielding a current on the order of several tens of μA that is proportional to the concentration of the overall available PS. From control experiments, the background current due to the redox activity of $(\text{NH}_4)_2\text{MoS}_4$ or $(\text{NH}_4)_2\text{MoO}_2\text{S}_2$ in the electrolyte under identical conditions was measured at or below $1.0 \mu\text{A}$. Therefore, any significant reduction in the magnitude of the current directly reflects a proportional reduction in the concentration of PS as a result of the reaction with the additives and hence acts as a probe in studying the PS uptake reaction kinetics. No sign of corrosion or other reactions were observed on the surface of the Monel electrodes by reactive sulfur species after extended hours of the chronoamperometric experiments, indicating the inertness of this electrode under the conditions of the test.

Cell fabrication and testing were performed in standard CR-2032 coin-cell format. In each case, sulfur was introduced into a carbon host (Bucky paper, 20 gsm) either through drop-casting from concentrated S/ CS_2 solution followed by melt-diffusion at $119 \text{ }^\circ\text{C}$ for 2 h, followed by additive loading, or by drop-casting from Na_2S_6 /ethanol solution on additive preloaded carbon host inside an Ar-filled glovebox. Additive loading into the carbon host was carried out by drop-casting saturated solutions containing $(\text{NH}_4)_2\text{MoS}_4$ or $(\text{NH}_4)_2\text{MoO}_2\text{S}_2$ in H_2O /acetonitrile (2 : 1 by volume), followed by evaporation of the solvent and drying under vacuum at $50 \text{ }^\circ\text{C}$ for a day. The obtained Sulfur/additive/carbon composite cathodes contain $\sim 4 \text{ mg S}$ ($\sim 60 \%$ by wt.) and $\sim 1 \text{ mg additive}$ ($\sim 14 \%$ wt.) in 7/16 inch diameter disks paired with $400 \mu\text{m}$ Li metal foil as the anode and Celgard as the separator, and was sealed with a measured volume of 1 M lithium bis(trifluoromethanesulfoniyl)imide (LiTFSI) in DOL-DME (1: 1) electrolyte containing 5% by weight LiNO_3 , to keep the electrolyte-to-sulfur ratio (E/S) at 10. Na-metal anode and 1 M

sodium perchlorate (NaClO_4) in TEGDME electrolyte containing 2 wt% NaNO_3 was used for Na-S cells. The cells were then cycled galvanostatically on an Arbin battery tester by applying a formation cycle at C/10 and subsequently at either C/5 or C/2 rate at room temperature.

Irrespective of the exact method of cathode preparation, consistent electrochemical results were obtained following the formation cycle. CV scans were on a BioLogic VSP potentiostat at a scan rate of 0.05 mV s^{-1} between the 1.8 and 3.0 V. EIS measurements were carried out from 1 MHz to 10 mHz with a 5 mV perturbation.

Theoretical calculations. Calculation of the spin-polarized electronic structures of the different species was carried out at the density functional theory (DFT) level using plane-wave basis sets with the Quantum Espresso (QE) code³⁷ and with projector augmented-wave (PAW) pseudopotentials, while the electronic exchange-correlation was modeled through generalized gradient approximation (GGA) as parameterized according to the Perdew-Burke-Ernzerhof (PBE) method.³⁸ The electronic kinetic energy was integrated at 544 eV cutoff, while the K-space was sampled at the Γ -point. In each simulation, the di-anionic $\text{Mo}_2\text{X}_2\text{S}_6^{2-}$ (X: O, S) and Sx^{2-} were charge-balanced by the addition of the Li^+ cations, placed in a dummy cubic cell with an edge of 20 Å, and treated as isolated species via application of the Martyna-Tuckerman correction scheme.³⁹ Calculations of the reaction activation energy were carried out with the climbing-image nudged elastic band (CI-NEB) module of the QE code, and the structures were considered relaxed when the total force was less than $0.1 \text{ eV}\cdot\text{Å}^{-1}$. Initially, the solvation effect in dioxolane was attempted by the implicit continuum solvation model using the Environ package.⁴⁰ However, this method was dropped later due to the oscillations in the electronic energy and convergence issues, and the transition-state geometries and energies were approximated *in vacuo*.

RESULTS AND DISCUSSION

The mixed-ligand $\text{MoO}_2\text{S}_2^{2-}$ dianion was obtained through $\text{O}^{2-}/\text{S}^{2-}$ ligand-exchange reactions from the isomorphous oxomolybdate MoO_4^{2-} , which is stable in aqueous solutions at high pH. The rapid $\text{O}^{2-}/\text{S}^{2-}$ ligand exchange and the accompanying sudden appearance of the orange color point to a fast reaction kinetics and the high affinity of the soft thio (S^{2-}) ligand toward the Mo center compared to the hard oxo (O^{2-}) counterpart, leading to the precipitation of phase-pure $(\text{NH}_4)_2\text{MoO}_2\text{S}_2$ according to reaction (1) and **Figure S1**. While the first and second oxo/thio ligand exchanges from MoO_4^{2-} to $\text{MoO}_2\text{S}_2^{2-}$ are fast, the third and fourth substitution reactions are considerably slower, hence separation of the phase-pure $\text{MoO}_2\text{S}_2^{2-}$ free from MoOS_3^{2-} and MoS_4^{2-} is feasible (**Figures S1 and S2**).²⁰



The resulting mixed-ligand $\text{MoO}_2\text{S}_2^{2-}$ and the full thio end member MoS_4^{2-} share some common electronic and structural properties. In both compounds, the hexavalent Mo center is tetrahedrally coordinated with chalcogenide ligands, with a ligand-to-metal charge-transfer (LMCT) that is responsible for the deep coloration of these complexes. The chemistry of MS_4^{2-} (M: Mo, W) and its interactions with S-containing species is well understood. For example, it has been reported that in solutions, MoS_4^{2-} has the tendency to dimerize into $\text{Mo}_2\text{S}_7^{2-}$ via bridging thio ligands with a concomitant reduction of one of the Mo centers and oxidation of its two terminal thio ligands into disulfido ligands (**Figure 1a**).^{20–23}

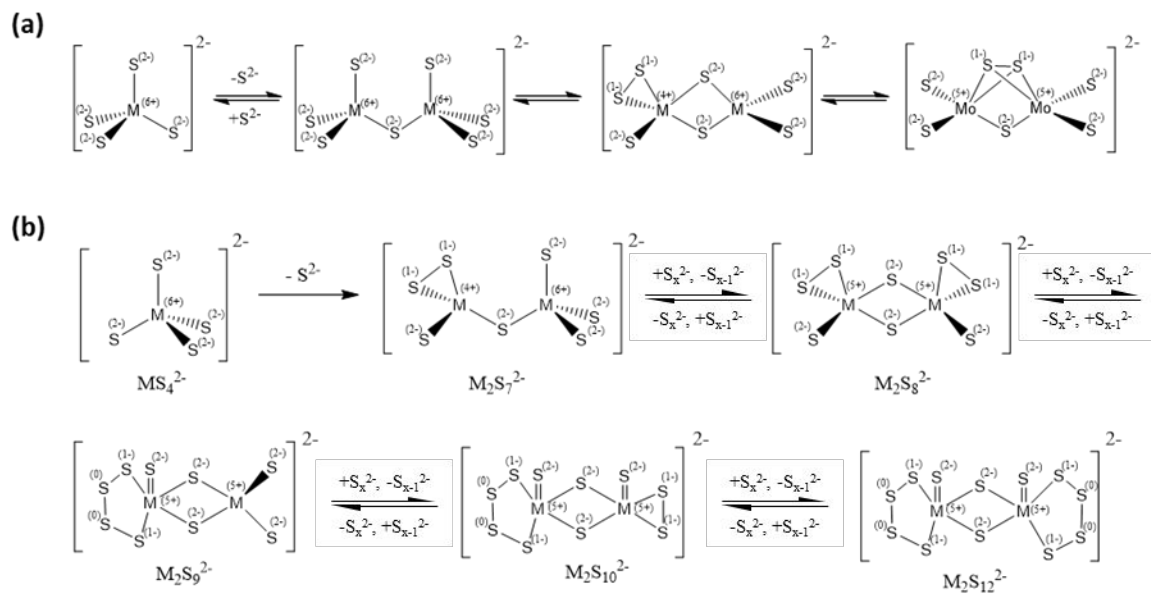


Figure 1. (a) Schematic representation of the dimerization and internal redox transformations observed in tetrahedral thiometallates, MS_4^{2-} (M: Mo, W). (b) The proposed pathway to dimerization and neutral S-atom addition to the dinuclear $M_2S_7^{2-}$ complex.

The internal redox reactions that occur during dimerization lead to the formation of a dinuclear complex with Mo-Mo homonuclear metallic bonding ($d = 2.45 \text{ \AA}$) and a high degree of electron delocalization as a result of Mo-Mo, Mo-S, and S-S covalent bonding. Therefore, the S ligands in $Mo_2S_7^{2-}$ are being activated for intermolecular redox reactions with foreign species, in particular molecules and ions with partially oxidized S atoms. A direct outcome of such reactions is that $Mo_2S_7^{2-}$ act as a reversible S-atom transfer reagent by incorporating S^0 -atoms in a stepwise manner to form complexes that have successively higher S/Mo ratios (**Figure 1b**).^{22–25}

Previously, it has been shown that either organo-polysulfide species such as dibenzyl trisulfide ($PhCH_2S_3CH_2Ph$) or elemental S can act as the S^0 -atom donor to the dinuclear Mo complex.²⁶ Nonetheless, as it is expected and demonstrated below, long-chain inorganic polysulfides, such as Li_2S_x ($4 \leq x \leq 8$) can also act as the source of the S^0 -atom during the above

reaction. This important aspect reveals the potentials of using the dinuclear Mo complexes with thio ligands as an additive to tackle the PS shuttle in S-batteries. In general, the solubility of the PS species in the ether-based electrolytes often used in S-batteries reduces with a shortening of the chain length (also equivalent to a further reduction of the average oxidation state on the S atoms and formation of more ionic species). As outlined in Figure 1b, the uptake of S-atom from polysulfides to the thio ligand network of the Mo dinuclear complex is accompanied by a partial reduction of the S atom from the polysulfide and partial oxidation of the thio/disulfido ligands to higher states that are mediated through Mo metal. The net outcome of such transformations is the shortening of the PS chain length in the electrolyte and its precipitation and suppression of the PS shuttle effect.

As the above redox transformations are mediated by the Mo-Mo center, intuitively, a change in the Mo coordination environment should induce measurable changes in the PS uptake reaction, both from thermodynamics and kinetics points of view. This is especially the case for the sequential reactions of S⁰-atom uptake when the formation of higher S/Mo ratios are sought via *ex situ* reactions (Figure 1b), as each step requires heating of the reagents to drive the reaction toward completion.²⁷ Since conventional S-batteries (such as Li-S and Na-S batteries) are to be designed to operate around room temperature, it would be of utmost importance to seek ways to increase the S-atom uptake reaction kinetics, should the dinuclear Mo complex be used as a homogeneous additive to suppress the PS shuttle in S-batteries.

In this regard, MoO₂S₂²⁻ emerges as a reasonable candidate to study the effect of ligand-exchange on the reaction kinetics of S-uptake by the Mo complex from the long-chain polysulfides. To monitor the course of the PS reaction with different Mo complexes under

conditions similar to that of a Li-S cell, chronoamperometry was used, as shown in **Figure 2**, while the schematic design of the electrochemical cell is given in **Figure S3**.

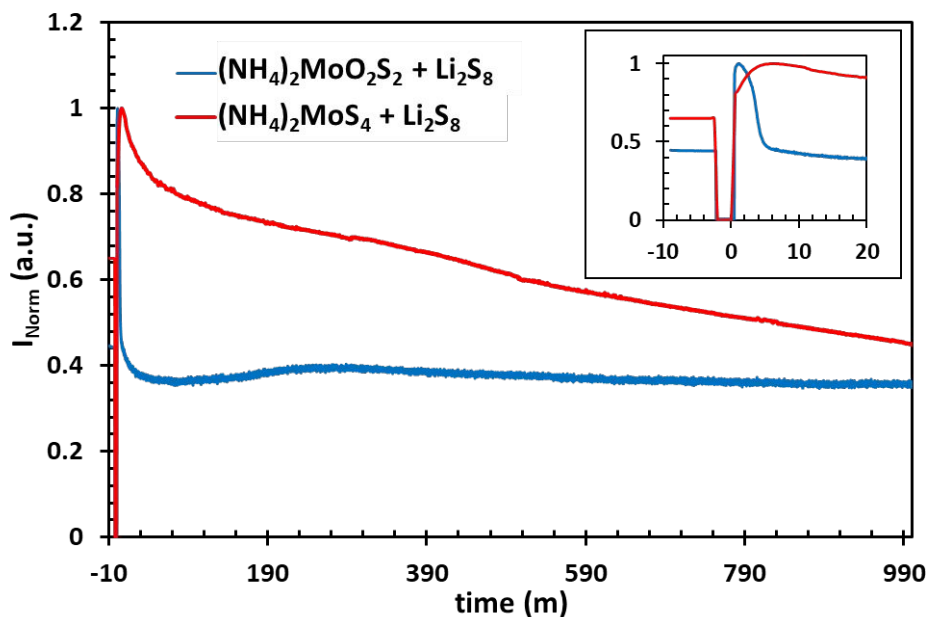
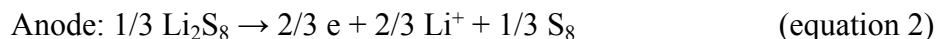
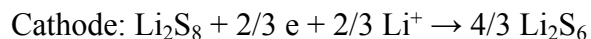


Figure 2. Chronoamperometric kinetic measurements of Li_2S_8 uptake by $(\text{NH}_4)_2\text{MoX}_2\text{S}_2$ (X: O, S). Measurements carried out at room temperature and an applied potential of 1.0 V. Inset shows an expanded view of the current evolution at the initial stages of the test.

It is to be noted that the glass cell in which chronoamperometric measurements were done is different from a conventional Li-S cell in that there is no Li anode or S cathode and only intermediate long-chain polysulfides exist in contact with a pair of inert, polarizable electrodes. Such a cell is designed specifically to exclusively study the homogeneous reactions between Mo-containing additives and polysulfide species in the electrolyte. As it can be seen from the inset in Figure 2, upon the addition of the solid $(\text{NH}_4)_2\text{MoX}_2\text{S}_2$ (X: O, S) additives to a 0.05 M $\text{Li}_2\text{S}_8/\text{DME-DOL}$ solution, the current rises rapidly to a maximum value. It is to be noted that in both cases, the background current observed at $t < 0$ (Figure 2 inset) originates from the redox interconversion of the Li_2S_8 species according to equation 2:



Following the initial measurement of the background current, the electrodes were removed from the cell to directly add the $\text{MoX}_2\text{S}_2^{2-}$ additives (and hence the null current). Immediately after the addition of the additives (Figure 2 inset, $t > 0$), the increase of the current to I_{max} (12 s for $(\text{NH}_4)_2\text{MoO}_2\text{S}_2$, 300 s for $(\text{NH}_4)_2\text{MoS}_4$) may be assigned to the formation of redox-active dinuclear complexes of Mo, while the subsequent decay is due to the S-atom uptake from the redox-active, long-chain Li_2S_8 species (Figure 1b) and the formation of shorter chain PS species that are less soluble in the ether-based electrolyte used. It is to be noted that: (i) due to the redox-active nature of the Mo-containing reaction products formed and (ii) the equilibrium behavior of reactions depicted in Figure 1b, there are always redox-active species in the electrolyte, contributing to a background current to flow indefinitely.

It is interesting to note the striking difference in the current decay rate after the addition of the two additives. While it takes only ~ 4 minutes in the case of $\text{MoO}_2\text{S}_2^{2-}$ additive to reduce I_{max} by about 65 % to a constant background, the reaction of MoS_4^{2-} with the soluble PS occurs at a considerably slower rate, reducing I_{max} by 55 % over the course of ~ 17 h. It is noteworthy that this large, enzymatic-level increase in the reaction rate was achieved only through an $\text{O}^{2-}/\text{S}^{2-}$ ligand exchange on the Mo center, pointing to a large stabilization of the transition-state electronic structure for the reactions outlined in Figure 1b (*vide infra*).

Before delving into the analysis of the transition-state structures, it is necessary to comprehend the underlying reaction mechanism that leads to a dimerization and S-atom uptake by the $\text{MoO}_2\text{S}_2^{2-}$ additive. To this end, a homogeneous reaction of $(\text{NH}_4)_2\text{MoO}_2\text{S}_2$ with elemental

S was employed in dimethyl formamide (DMF) at 85 °C to simulate the formation of possible reaction products in an actual Li-S cell with $\text{MoO}_2\text{S}_2^{2-}$ additive and reactive polysulfides, as DMF, unlike DOL-DME, has a high solubility for $(\text{NH}_4)_2\text{MoO}_2\text{S}_2$. Also, previously our group showed that high donor number, N-containing solvents such as N,N-dimethylacetamide favors the formation of trisulfide radical anion $\text{S}_3^{\cdot-}$ from long-chain PS species.²⁸ In an attempt to avoid a drastic change in the reaction mechanism by the $\text{S}_3^{\cdot-}$ that forms in DMF, Li_2S_8 was replaced with elemental S as the S-atom source, which is closest in oxidation state to Li_2S_8 (respectively, 0 vs. -0.25) and at the same time has a relatively high solubility in hot DMF.

The crystal structure of the $\text{MoO}_2\text{S}_2^{2-}$ —S₈ reaction product described above was solved through single-crystal X-ray diffraction and is presented in **Figure 3**, while the crystallographic data, atomic coordinates, anisotropic atomic displacement parameters, and selected bond-lengths are given, respectively, in **Tables S1** through **S4**. In general, the structure is composed of a dimerized homonuclear complex of Mo connected through two bridging sulfide ligands and a Mo-Mo bonding (d: 2.8281(7) Å), where each Mo receives further coordination from a terminal oxo ligand and either a bidentate disulfido or tetrasulfido ligands, giving rise to the structural formula $[(\eta\text{-S}_2)\text{Mo}_2\text{O}_2(\mu\text{-S})_2(\eta\text{-S}_4)]^{2-}$ (**A**) for the dianion.

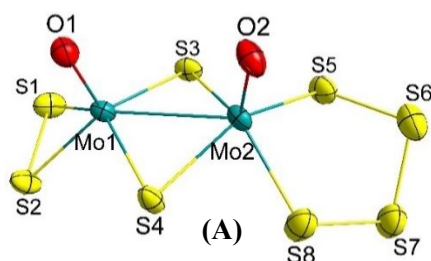


Figure 3. Single-crystal XRD structure of the dianionic $[(\eta\text{-S}_2)\text{Mo}_2\text{O}_2(\mu\text{-S})_2(\eta\text{-S}_4)]^{2-}$ complex (compound A) formed as a result of the reaction between $\text{MoO}_2\text{S}_2^{2-}$ and S. The two $(\text{CH}_3)_4\text{N}^+$ cations and CH_3CN crystal solvent are not shown for clarity.

The structure of **A** was also reported previously as a homogeneous catalyst for hydrogen evolution reaction (HER) via a one-pot synthesis starting from an aqueous PS solution and MoO_4^{2-} as the Mo source.¹⁹ As in the current case we managed to obtain **A** through a stepwise reaction starting from $\text{MoO}_2\text{S}_2^{2-}$ as the only source of Mo, clear mechanistic conclusions can be drawn regarding the dimerization of the Mo centers and the subsequent polysulfide uptake. First, the lower O/Mo ratio in **A** compared to that in the $\text{MoO}_2\text{S}_2^{2-}$ building block implies an atomic disproportionation mediated through an internal electron-transfer, followed by an external redox reaction (oxidation) and finally dimerization as depicted in **Figure 4a** and also as proposed previously.²⁹

Therefore, the mixed-anionic, dinuclear $[\text{Mo}_2\text{O}_2(\mu\text{-S})_2(\eta\text{-S}_2)_2]^{2-}$ (**B**) forms as an intermediate and the first member of the subsequently heavier S/Mo complexes that are active for S-atom uptake from the soluble polysulfides. The structure of **B** has been reported previously, obtained from alkaline aqueous-phase reactions involving $(\text{NH}_4)_2\text{MoO}_2\text{S}_2$ and $[(\text{CH}_3)_4\text{N}]\text{Cl}$ at the boiling temperature in the air.³⁰ As a major point of contrast, it is to be noted that in our case, the reaction occurred under strictly dry conditions, indicating that atomic disproportionation leading to the formation of **B** can also happen from nonaqueous solvents, similar to the electrolytes employed in S-batteries.

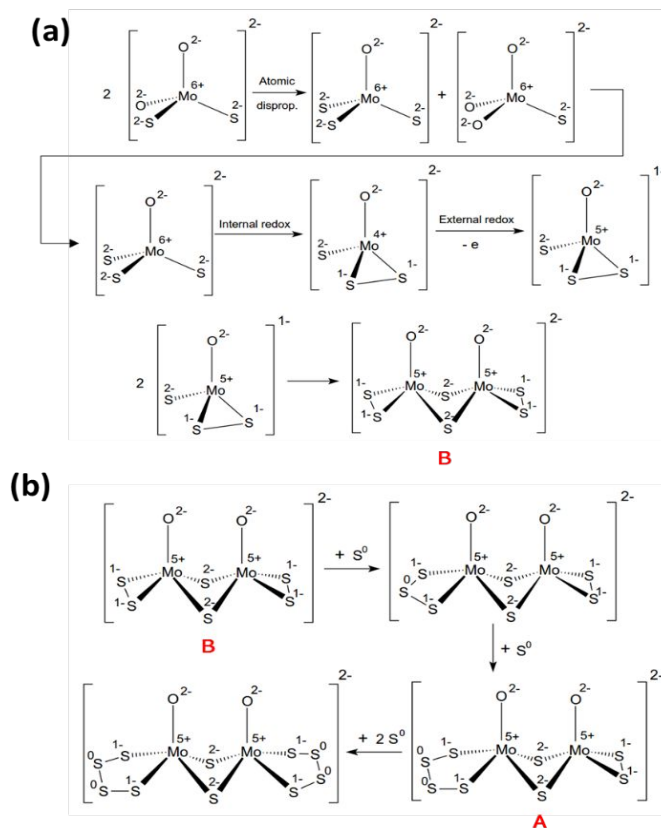


Figure 4. (a) The proposed mechanism for the formation of the dinuclear $\text{Mo}_2\text{O}_2\text{S}_6^{2-}$ complex (compound **B**) starting from $\text{MoO}_2\text{S}_2^{2-}$ as the building block. (b) Schematic representation of the neutral S-atom uptake from polysulfides and formation of heavier complexes. Compound **A** separated and identified with X-ray crystallography.

Following the formation of compound **B**, $\text{Mo}_2\text{O}_2\text{S}_6^{2-}$, which is isostructural and analogous to the all-sulfur counterpart $\text{Mo}_2\text{S}_8^{2-}$, S-atom addition from oxidized sulfur can happen (**Figure 4b**), yielding the higher S/Mo complexes and ultimately, $\text{Mo}_2\text{O}_2\text{S}_{10}^{2-}$. It is believed that the eventual S-atom uptake and formation of the heavier $\text{Mo}_2\text{O}_2\text{S}_x^{2-}$ complexes are the major cause of the fast current decay observed during the chronoamperometric analyses (Figure 2).

From a chemical point of view, a drastic increase in the reaction rate obtained via the $\text{O}^{2-}/\text{S}^{2-}$ ligand exchange implies a significant reduction in the energy of the transition-state structure.

In order to probe the reaction mechanism, the structure of the transition-state was optimized at the density functional theory (DFT) level using Nudged Elastic Band (NEB) method. Details of the theoretical calculations, along with the choice of the reactants and products, are provided in the Methods section. Among many possibilities, the reaction presented in equation 3 was used to obtain the geometry of the transition-state:



The choice of $\text{S}_3^{\cdot-}$ as the major reaction product for this step is that $\text{S}_3^{\cdot-}$ has proven to exist in a variety of solvents at equilibrium with long-chain PS and is often the reactive form of sulfur.^{31–34} The cross-sections of the potential energy surface along the reaction coordinates are shown in **Figure 5a** for the two instances of the dinuclear complex with oxo and thio ligands. It is evident that for the reaction depicted in equation 3, DFT predicts an activation energy of 1.21 and 0.54 eV, respectively, for X : S and O. It is to be noted that while solvation has significant effects on stabilization of the transition-state energy and only gas-phase bimolecular reactions are assumed for DFT purpose, the calculations reflect the lower activation energy of the $\text{Mo}_2\text{O}_2\text{S}_6^{2-}$ additive in comparison to the $\text{Mo}_2\text{S}_8^{2-}$ analog in the S-atom transfer reaction.

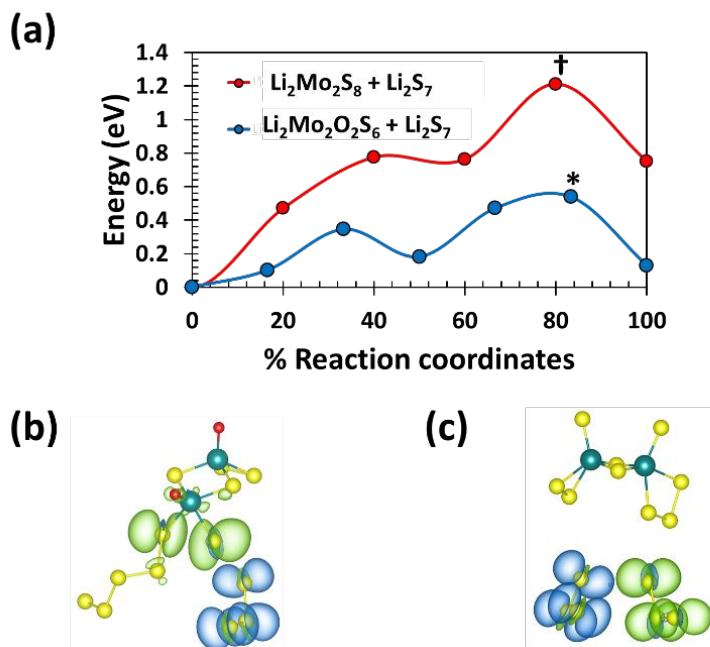


Figure 5. (a) DFT calculations of the activation energy for the S⁰-atom uptake reaction by Mo₂X₂S₆²⁻. The cross-section of the potential energy surface (PES) at the minimum energy path for the reaction described in equation 3, indicating the calculated activation energies for the neutral S-atom uptake from S₇²⁻ by the Mo₂X₂S₆²⁻ additives (X: O, S). In each case, the transition-state energy (saddle-point in the PES) is marked with, respectively, a dagger and an asterisk. (b) and (c) show the electron spin density surface plotted for the transition-state structure for the Mo₂X₂S₆²⁻ + S₇²⁻ reaction for, respectively, X: O, and X: S.

The reaction path obtained through DFT calculations can be further interrogated to find clues into the origins of the large energy difference in the energy of the transition-state brought about by O/S ligand exchange. To this end, the optimized electronic structures at the transition-state (marked with a dagger and a star in Figure 5a) were used for extraction of the electron spin polarization density maps, as shown in Figure 5b. The high value of electron spin density implies the high probability of finding an unpaired electron in a given volume of space. Hence, from Figure 5b, it is evident that at the transition-state of Mo₂S₈²⁻ + S₇²⁻ reaction, the majority of the unpaired electron density is on the S₃⁻ products (equation 3), while the Mo₂S₉²⁻ product has essentially the incoming S-atom incorporated into the disulfido ligands, with all the electrons

paired in the dinuclear complex. This is in sharp contrast with the $\text{Mo}_2\text{O}_2\text{S}_6^{2-} + \text{S}_7^{2-}$ reaction intermediate in which part of the unpaired electron density penetrates the dinuclear complex. In this case, the transition-state involves dissociation of the S—S bond in the disulfido ligand (Figure 4a, compound **B**) and the formation of a diradical. Also, some of the electron spin is also transferred to the Mo $4d$ and O $2p$ molecular orbitals, indicating the strong inductive effect of the oxygen ligand in dissociating the S—S bond. The above arguments and the proposed drastic change in the reaction mechanism incurred as a result of O/S ligand exchange on the Mo complex are represented schematically in **Figure 6**.

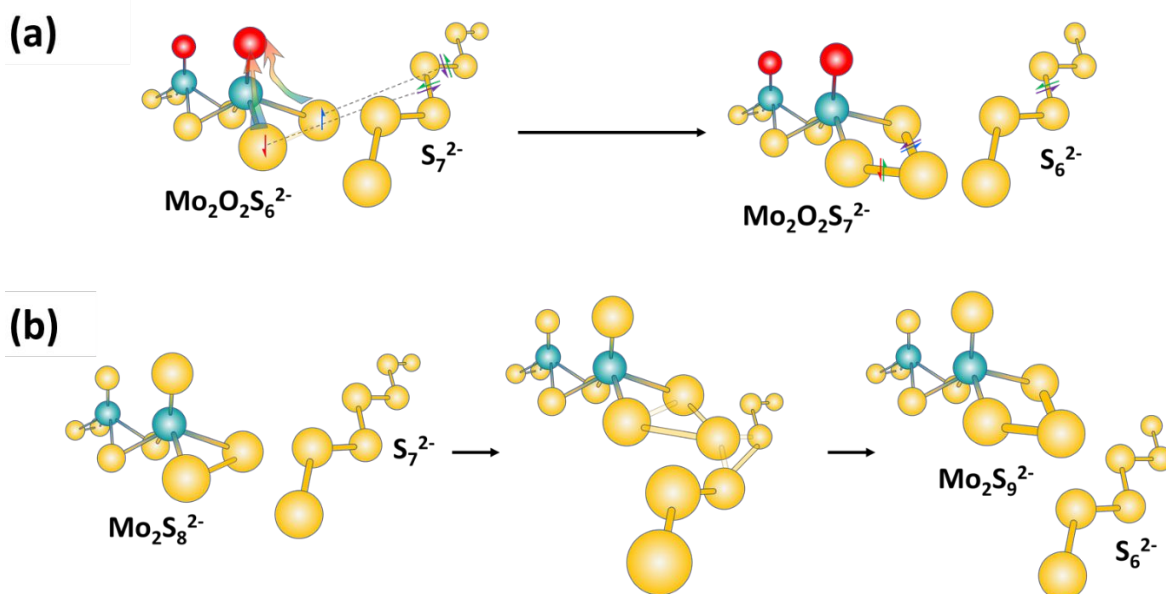


Figure 6. The effect of the O/S ligand exchange on the $\text{Mo}_2\text{X}_2\text{S}_6^{2-}$ complex (X: O, S) on the S^0 -atom uptake reaction mechanism. **(a)** Schematic representation of the radical reaction pathway in $\text{Mo}_2\text{O}_2\text{S}_6^{2-}$ complex with the polysulfide. **(b)** Schematic representation of the closed-shell reaction pathway in $\text{Mo}_2\text{S}_8^{2-}$ complex with polysulfide.

From the above theoretical predictions, it implies that the higher polysulfide uptake reaction rate observed with the oxo-substituted dinuclear complex is due to the formation of a low-energy radical intermediate. To test this assertion experimentally, the reaction of

$(\text{NH}_4)_2\text{MoX}_2\text{S}_2$ (X: O, S) with Li_2S_6 was monitored spectrophotometrically in DMSO solvent. It is known that the PS species have the tendency to dissociate into $\text{S}_3^{\cdot-}$ in high donor number solvents, including DMSO.²⁸ This can be readily verified as a solution of Li_2S_8 in DMSO gives rise to a peak at 618 nm, corresponding to the electronic transitions in the $\text{S}_3^{\cdot-}$ species (**Figure 7a**). Therefore, monitoring the solution absorbance at this wavelength versus time provides direct kinetic information regarding the reaction rate. As shown in **Figure 7b**, there is a rapid decline in the concentration of $\text{S}_3^{\cdot-}$ as a solution of $(\text{NH}_4)_2\text{MoO}_2\text{S}_2$ in DMSO is spiked in. The absorbance follows a non-linear decay from 1.25 to 0.4 within 2,400 s, indicating a complex and multi-step reaction mechanism. On the other hand, $\text{S}_3^{\cdot-}$ reaction with $(\text{NH}_4)_2\text{MoS}_4$ follows at much slower rates with non-monotonic oscillations, indicating higher activation energy compared to that of the oxo-analog. These observations corroborate the DFT predictions, indicating a low-energy radical reaction mechanism for the $\text{S}_3^{\cdot-}$ — $(\text{NH}_4)_2\text{MoO}_2\text{S}_2$ reaction, while a spin-paired mechanism for the $\text{S}_3^{\cdot-}$ — $(\text{NH}_4)_2\text{MoS}_4$ reaction.

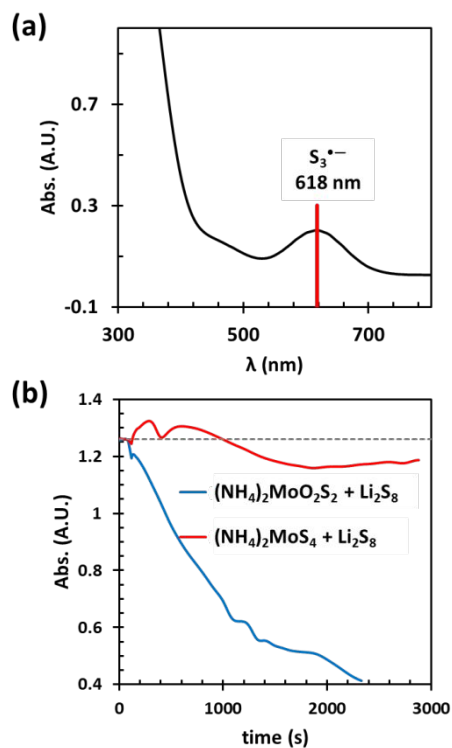


Figure 7. Propensity of the radical S^0 -atom uptake reaction pathway between $\text{Mo}_2\text{X}_2\text{S}_6^{2-}$ and $\text{S}_3^{\bullet-}$. **(a)** The optical absorption spectrum of a 0.01 M solution of Li_2S_8 in DMSO, indicating an absorption band at 618 nm due to the $\text{S}_3^{\bullet-}$ species. **(b)** Chronophotometric monitoring of the $(\text{NH}_4)_2\text{MoX}_2\text{S}_2$ (X: O, S) reaction kinetics with $\text{S}_3^{\bullet-}$ at 618 nm in DMSO.

Finally, XPS analysis was utilized to assess the validity of the reaction depicted in Figure 1b, as shown in **Figure 8**.

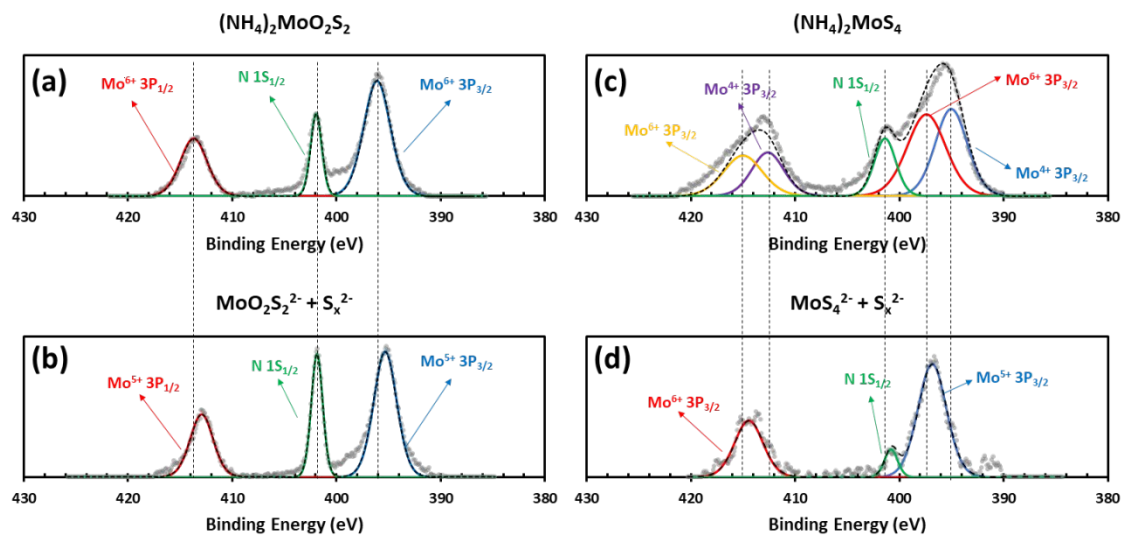


Figure 8. Observed and deconvoluted Mo 3p XPS spectra of (a) pure $(\text{NH}_4)_2\text{MoO}_2\text{S}_2$, (b) $(\text{NH}_4)_2\text{MoO}_2\text{S}_2$ reacted with polysulfide, (c) pure $(\text{NH}_4)_2\text{MoS}_4$, and (d) $(\text{NH}_4)_2\text{MoS}_4$ reacted with polysulfide.

From Figure 8, one can see that the reaction of $\text{MoO}_2\text{S}_2^{2-}$ with long chain polysulfides is accompanied by a red-shift in the position of the Mo $3p_{3/2,1/2}$ transitions (panels (a) and (b)), indicating a reduction in the oxidation state of Mo from the initial valence of 6+ in $\text{Mo}^{6+}\text{O}_2\text{S}_2^{2-}$ to 5+ in the dinuclear complex, as indicated in Figure 1b. For the pristine $(\text{NH}_4)_2\text{MoS}_4$ (panel (c)), the Mo 3p XPS spectrum is more complicated as the commercial product contains some surface Mo^{4+}S_2 impurity that is probed by the surface-sensitive XPS technique. Hence, the observed spectrum is a convoluted pattern of Mo $3p_{3/2,1/2}$ electronic transitions superimposed for the two oxidation states of Mo. As shown in panel (d), the reaction of MoS_4^{2-} with the long-chain polysulfide yields reduced Mo species (please note that MoS_2 is insoluble in the electrolyte and hence does not react with the polysulfide). In panels (a) through (d) of Figure 8, the peak at 402

eV binding energy corresponds to the N 1s orbitals (as NH_4^+ cations) and hence provides an internal standard to verify the red-shifts in Mo 3p transitions to the lower oxidation states as a result of dimerization and S-atom transfer, as presented in Figure 1b.

Finally, Figure 9 (a) and (b) present the XPS spectra of Mo and N species that form as SEI on the surface of Li anode after few cycles of the Li-S cells. The presence of two N species originates from the co-existence of various oxidation states of N, *i.e.*, N^{3+} from partially reduced NO_3^- (electrolyte additive) and neutral and reduced nitrogen due to, respectively, the N-C bonds of TFSI electrolyte salt and nitrides. As the Mo 3p transition is concerned, the XPS spectra show the presence of both Mo^{6+} and Mo^{4+} , indicating the partial reduction of the Mo species into MoS_2 and incorporation of these mixed-state Mo species into the structure of the anode SEI. Thus, it is anticipated that Mo-based additives play two chemical roles when introduced as electrolyte additives in Li-S cells: (i) reaction with polysulfides and formation of dinuclear complexes, and (ii) reaction at the Li surface and incorporation into the Li anode SEI. To further probe the effect of Mo-based additive on the electrodeposition of Li anode, SEM images of the Li anode were obtained from post-mortem analysis of Li-S cells (**Figure 9(c)-(e)**). Evidently, the lack of any Mo-based liquid-phase additive leads to a highly non-uniform dendritic growth of Li in the fail-fast cells as expected (panel (a)). However, in both cells with Mo-containing additive (panels (c) and (d)), the Li surface shows much smoother geometry, indicating a suppression of the dendrite growth and stabilization of Li electroplating. The observed smooth Li anode surface is a direct consequence of having Mo species incorporated into the structure of the SEI, in agreement with the XPS studies.

As discussed above, the $\text{Mo}^{(4+)}\text{S}_2$ species formed as a result of the reductive decomposition of $\text{MoX}_2\text{S}_2^{2-}$ species on the surface of Li deposits acts as an artificial SEI, which has both

appreciable Li^+ diffusivity and at the same time high stability due to the strong Mo-S covalent bonds. Such SEI additives seem to reinforce the resistance of the Li toward unwanted side reactions with the reactive polysulfide species that are present in the electrolyte. Finally, it is evident that $\text{MoO}_2\text{S}_2^{2-}$ leaves a smoother Li finish compared to the MoS_4^{2-} counterpart, indicating that the faster reaction kinetics of the former with polysulfides is reflected also in the more favorable surface topology of the Li anode. In order to further interrogate the MoS_2 -containing SEI, further XPS spectra were recorded from the surface of Li after 1,000 s of Ar-ion sputtering, equivalent to about 400 nm of depth profiling. The results of XPS deconvolution and curve fittings of $\text{MoO}_2\text{S}_2^{2-}$ and MoS_4^{2-} (**Figure S5a and b**) indicate a higher relative signal intensity for MoS_2 in the oxo/thiomolybdate compared to the MoS_4^{2-} . This observation directly corroborates the superior protection of Li surface and smoother finish of Li electrodeposition with $\text{MoO}_2\text{S}_2^{2-}$.

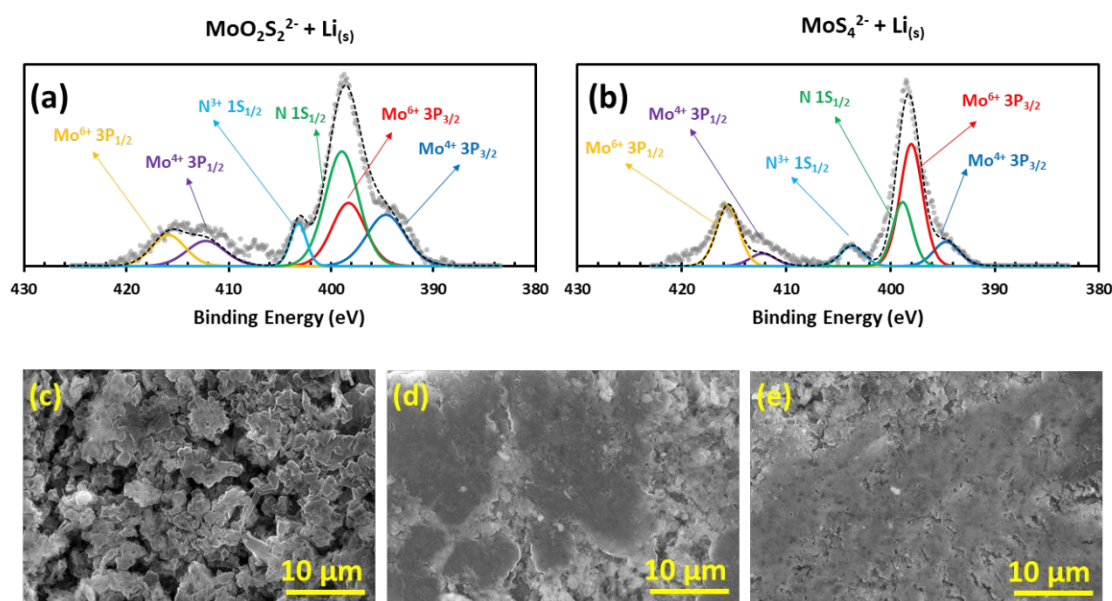


Figure 9. Observed and deconvoluted Mo 3p XPS spectra of (a) $(\text{NH}_4)_2\text{MoO}_2\text{S}_2$ reacted at the surface of Li anode and (b) $(\text{NH}_4)_2\text{MoS}_4$ reacted at the surface of the Li anode. Post-cycling SEM micrographs of the Li anode surface in, respectively, (c) blank, (d) MoS_4^{2-} , and (e) $\text{MoO}_2\text{S}_2^{2-}$ added Li-S cells.

Given the observed enzymatic-level increase in the reaction rate observed through O/S ligand exchange on the Mo center in the dinuclear complex and the improved suppression of the dendritic growth of Li in Mo-treated electrolytes, it is necessary to inspect the impact of the faster PS uptake on the cell performance in S-batteries. **Figure 10a** shows the electrochemical impedance spectra (EIS) of cells following the first formation cycle, with the values of the fitted parameters presented in **Table S5** (The EIS curves for the pristine cells are given in **Figure S6**). All spectra can be fitted with two R|CPE elements in series (CPE is the constant-phase element and a non-ideal capacitor), where the two semicircles represent the charge-transfer (CT) resistance for the anodic and cathodic reactions, respectively. From the fitting results (Table S5) and the values of CPE-T (capacitance), it is possible to assign R2|CPE1 to the cathodic CT resistance (polysulfide redox chemistry), while R3|CPE2 represents the anodic CT resistance (lithium electrodeposition). This assignment is based on the fact that the carbon cathode has a higher capacitance than the Li anode and also, R2 values for the cells treated with the additives are significantly lower than that of the blank cell, so that R2|CPE1 represent the charge-transfer at the cathode-electrolyte interface. According to the EIS results, the addition of Mo-based species heavily reduces mainly R2 and R3 (in the case of $\text{MoO}_2\text{S}_2^{2-}$), leading to a considerable reduction of the cell impedance compared to the blank cell. The reduction of R3 (anodic CT resistance) appears to corroborate well with the smooth and thin-SEI finish of Li surface, as observed through the SEM micrographs (Figure 9c). On the other hand, the reduction in R2 (cathodic CT resistance) is indicative of low-resistance and reversible redox chemistry of S-containing Mo-species, formed as suggested in Figure 1b. These results on one hand consolidate the S-atom uptake by Mo-containing species, as otherwise similar R2 values should be observed in blank cells and those treated with additives. Furthermore, we can conclude that the O/S ligand

ex-change in $\text{MoO}_2\text{S}_2^{2-}$ additive also considerably reduces the activation energy in S/S^{2-} redox activation energy, as observed through the drastic reduction in R2 CT resistance. This assertion is further verified by the cyclic voltammetry (CV) and galvanostatic charge-discharge curves (Figure 10 (b) and (c)), as both represent obvious reduction in charge and discharge overpotentials compared to the blank cell. In Figure 10(b), the larger cathodic peak at 2.00 V (and the corresponding anodic peak at 2.3 V) represents the reduction (oxidation) of long-chain polysulfides to shorter chain polysulfides and eventually Li_2S , while the smaller cathodic peak at 2.3 V and the corresponding anodic peak above 2.4 V represent, respectively, reduction of S to long-chain polysulfides and the reverse process. The same argument applies to other systems in Figure 10(b). From Figure 10(d), it appears that the improvement in cell kinetics and smooth Li electrodeposition surface geometry is compromised by a reduction in first-cycle capacity, an indication of the lower utilization of S cathode due to its partial incorporation into Mo-containing complexes.

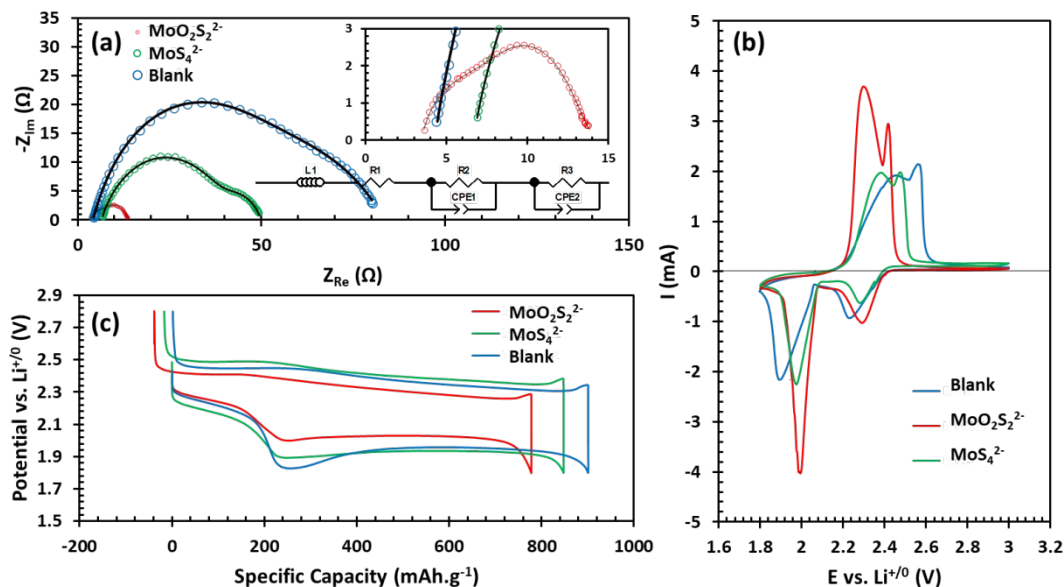


Figure 10. Electrochemical characterization of the Li-S cells with and without various $\text{MoX}_2\text{S}_2^{2-}$ additives. **(a)** Electrochemical impedance spectra after an initial cyclic voltammetry formation cycle. Open symbols represent observed datapoints and the solid-line is the fitted curve. The inset shows an expanded view of the low impedance region and representation of the Randles circuit used for fitting. **(b)** 1st cycle cyclic voltammetry curves at 0.05 mV s^{-1} scan rate. **(c)** 1st cycle voltage-composition profiles from galvanostatic charge-discharge curves at $C/5$.

Finally, the effect of the O/S ligand exchange on the performance improvement of Li-S cells is shown in **Figure 11** for fail-fast coin-cells with high S loading ($\sim 4 \text{ mg S.cm}^{-2}$) and lean electrolyte ($E/S = 10 \text{ } \mu\text{L.mg}^{-1}$) cycled at $C/5$. It is well understood that utilization of high mass loading of S in combination with limited amounts of the electrolyte aggravates premature cell failure. Also, the use of an open carbon fiber network (bucky paper) with a macroporous structure, such as the one used here, further exacerbates the cell failure as the long-chain polysulfide formed during the cell operation are readily released into the electrolyte in the absence of a meso- or microporous carbon network to trap them, and can freely diffuse onto Li anode and initiate SEI growth and polysulfide shuttle (an SEM image of the blank bucky paper used as carbon host in this work is given in **Figure S7**). Therefore, it is to be re-emphasized that the cells used in the evaluation of the Mo-containing additives are engineered to fail early, and

not meant to be optimized for long cycling. Such fail-fast systems are used routinely in industrial process to demonstrate the extreme case scenarios and the efficacy of possible remedies under highly demanding conditions. In the current case, the Li-S cell failure is happening through elevated PS/Li side-reactions, growing of a thick Li-electrolyte SEI, and enhanced Li dendritic growth leading to electrolyte consumption and catastrophic anode-cathode short contacts. This very expected behavior is demonstrated in the cycle-life retention of the blank cell assembled with no additive in Figure 11a (red trace), where despite a relatively high initial specific capacity of 1130 mAh.g^{-1} ($\sim 65\%$ S utilization), the cycle-life ends abruptly following an internal short contact between the electrodes following 100 cycles. On the other hand, the cell with $(\text{NH}_4)_2\text{MoO}_2\text{S}_2$ additive delivers a lower initial capacity of 780 mAh.g^{-1} (47% S utilization), but is stable over the next 170 cycles (83% capacity retention) under the above highly unoptimized cell conditions with a decline evident afterward, indicating 80% improvement in the deliverable energy over extended cycling. Finally, while the cell with $(\text{NH}_4)_2\text{MoS}_4$ additive effectively suppresses the catastrophic failure and premature cell death, it undergoes rapid capacity loss following the 50th cycle, yielding 29% capacity retention after 200 cycles. The obvious difference in cycle-life retention, also summarized as normalized capacities in Figure 11a inset, emphasizes the importance of the PS uptake kinetics, improved sulfur redox kinetics, and improved Li deposition surface morphology when homogeneous additives are used to regulate the concentration of the reactive sulfur in the electrolyte of the Li-S cells. While PS-reactive additives are in general effective in alleviating the abrupt cell death, an additive with fast reaction kinetics is essential to improve the extent of PS uptake, especially in high-power applications where PS species are generated at a higher rate.

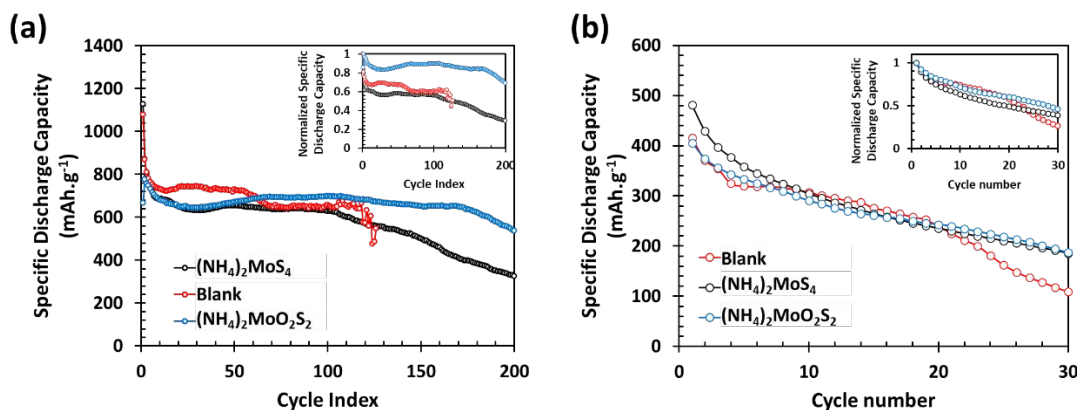


Figure 11. The effect of Mo-based additives on the electrochemical performance of S-based batteries. **(a)** The cycle-life performance of Li-S cells with $(\text{NH}_4)_2\text{MoX}_2\text{S}_2$ (X: O, S) additives, as compared to a blank cell with no additive. **(b)** The cycle-life performance of Na-S cells with $(\text{NH}_4)_2\text{MoX}_2\text{S}_2$ (X: O, S) additives, as compared to a blank cell with no additive. In both panels, insets exhibit the normalized specific discharge capacities.

In addition to the cycle-life retention, it is also instructive to note the differences in the coulombic efficiency (CE) as $\text{MoX}_2\text{S}_2^{2-}$ additives are introduced into Li-S cells (Figure S4). For the blank cell, the CE starts from a high of 103.0 % and ends in 98.3 %, just before the catastrophic cell failure after 100 cycles. On the other hand, the cells loaded with $\text{MoX}_2\text{S}_2^{2-}$ additives show significantly lower than 100 % CE, indicating some extra faradaic reactions on top of the regular PS shuttle. It is anticipated that the dinuclear complexes that form from thiomolybdate species can get partially reduced on the anode, which can reversibly get oxidized on the surface of the cathode, causing their regeneration. For the MoS_4^{2-} additive, CE starts at a high value of 102.5 % and ends in 94.2 % after 200 cycles. For the $\text{MoO}_2\text{S}_2^{2-}$ additive, CE starts at 95.3 % and finishes at 90.8 % after 200 cycles. Here, it has been shown that maintaining a high deliverable capacity and suppressing PS shuttle is accompanied by a poorer CE than the ideal value, caused by the higher reactivity of $\text{MoO}_2\text{S}_2^{2-}$, compared to MoS_4^{2-} , which are together less efficient than the blank cell. Admittedly, these results indicate a compromise that needs to be

made to improve the performance and improved safety of the Li-S cells under demanding high mass-loading sulfur and lean electrolyte conditions. Nonetheless, we anticipate that the utilization of homogeneous-phase additives is in its early stages of development, and future advances requires pairing with Li artificial SEI formation and protection, such as our previous work using Te-based species^{35,36}, in order to reach a multicomponent strategy to tackle the PS shuttle in Li-S batteries.

The reactivity observed for the $\text{MoX}_2\text{S}_2^{2-}$ building blocks with PS species is supposedly a universal behavior that can occur under different solvent environments. As such, these spontaneous reactions can be exploited as a general strategy in the treatment of the PS shuttle problem in different metal—sulfur batteries, thereby increasing their impact on broad range of S-based batteries beyond just Li-S batteries. As the closest analog to the Li-S cells, Na-S cells were also treated with the $\text{MoX}_2\text{S}_2^{2-}$ additives to study the effect on the cell performance, and the results are given in **Figure 11b**. It is to be noted that the performance of the Na-S cells is considerably more susceptible to uncontrollable side reactions beyond their Li counterpart. One major reason for such poor performance is the electrodeposition of Na metal, which is prone to excessive electrolyte reduction at the metal/electrolyte interface and the formation of thick, ion-blocking layers that passivate the Na metal. Therefore, compared to the Li-S chemistry, the PS shuttle plays a proportionally smaller role in cell capacity fade. Nonetheless, the effect of the soluble Mo-based additives in regulating PS concentration in the electrolyte is visible, as shown in Figure 11b. As expected, all cells lose a significant fraction of the initial capacity due to the Na-metal surface deactivation. However, the cells with the thiomolybdate derivatives demonstrate differential improvements in cell performance by slowing down the rate of capacity fade. Among the two $\text{MoX}_2\text{S}_2^{2-}$ additives used, MoS_4^{2-} shows a higher initial capacity similar to

the Li anode cells (Figure 10c). On the other hand, the cells with $\text{MoO}_2\text{S}_2^{2-}$ additive demonstrate slightly better capacity retention, as shown by the normalized capacity in the inset of Figure 11b. While the improvements in cycle-life retention observed for the Na-S cells are considered minor, it can potentially open an avenue for future works as better solutions are invented to circumvent the unstable Na-electrolyte interfacial SEI.

CONCLUSIONS

In this work, it has been shown how homogeneous, electrolyte-soluble additives based on mixed-ligand molybdenum compounds can be used as a strategy to diminish the problem of soluble polysulfide species in sulfur-based batteries. In general, it has been shown that the spontaneous condensation of the tetrahedral $\text{MoX}_2\text{S}_2^{2-}$ (X: O, S) species and internal redox reactions, followed by partial reduction of the Mo center and oxidation of the thio to disulfido ligands, creates dinuclear complexes with metallic Mo-Mo bonding. On one hand, these dinuclear complexes are labile toward oxidized sulfur (S^0) species, undergoing S-atom transfer from the polysulfides into the dinuclear complex structure, effectively lowering the concentration of the reactive polysulfides in the electrolyte and reducing the charge-transfer resistance in polysulfide redox interconversion reaction. On the other hand, the electrolyte-soluble oxo/thio molybdates and, in particular $\text{MoO}_2\text{S}_2^{2-}$, reacts at the surface of Li anode to deposit a dense solid-electrolyte interface that protects the anode surface from dendritic growth of the Li metal and reduces the overpotential for Li electrodeposition. The suppression of the polysulfide concentration in the cell along with the smooth Li electrodeposition finish is reflected directly in a significant improvement of the cell performance by diminishing the chances of anode-cathode short contacts and slowing down the rate of capacity fade in fail-fast Li-S cells. In particular, it

has been discovered that a ligand exchange from thio (S^{2-}) to oxo (O^{2-}) on the tetrahedral Mo center in the $MoX_2S_2^{2-}$ building block imparts enzymatic level activities to the dinuclear complex in polysulfide uptake reactions, increasing the reaction rate by about two orders of magnitude. Atomistic kinetic calculations at the density functional theory level indicated that through inductive effects in the $[Mo_2O_2(\mu-S)_2(\eta-S_2)]^{2-}$ moiety, oxo ligand favors dissociation of the disulfido bond coordinated to the common Mo center in the dinuclear complex into a diradical, thus reducing the activation energy for the transition-state by about 0.7 eV compared to the full thio analog $[Mo_2S_2(\mu-S)_2(\eta-S_2)]^{2-}$. The faster polysulfide uptake rate with the oxo-complex is clearly reflected in the better capacity retention of Li-S coin-cells with high mass loading of S and limited amounts of electrolyte (80 %) compared to the thio-complex (29 %) after 200 cycles, which are in striking contrast with the blank cell devoid of any additive (catastrophic failure after 100 cycles). Finally, the homogeneous additive strategy involving the thiomolybdate additives was also tested in Na-S cells, where both additives showed promising results in slowing down the rate of capacity fade, despite that Na-metal deactivation and SEI build-up are still dominating the overall cell death. Overall, the strategy of using homogeneous additives to regulate the concentration of the polysulfides in the electrolyte is expected to create a new dimension in solving the fundamental problems of sulfur-based batteries, driving them one step closer to realization. This can constitute an important step in the transition from fossil fuels to electrification and renewable energy utilization using earth-abundant and environmentally friendly chemistries.

DATA AVAILABILITY

The data sets supporting this article have been uploaded as part of the electronic supplementary information (ESI).†

AUTHOUR INFORMATION

*Corresponding author

Arumugam Manthiram — *Materials Science and Engineering Program and Texas Materials Institute, The University of Texas at Austin, Austin, Texas, USA; orcid.org/0000-0003-0237-9563; Email: manth@austin.utexas.edu*

Authors

Hooman Yaghoobnejad Asl— *Materials Science and Engineering Program and Texas Materials Institute, The University of Texas at Austin, Austin, Texas, USA; orcid.org/0000-0003-4021-5025; Email: hynr8@mst.edu.*

Amruth Bhargav— *Materials Science and Engineering Program and Texas Materials Institute, The University of Texas at Austin, Austin, Texas, USA; orcid.org/0000-0002-1793-8340; Email: amrubhar@utexas.edu*

CONFLICTS OF INTEREST

The authors declare no competing financial interest.

†Electronic supplementary information (ESI) available: XRD pattern of the as-synthesized $(\text{NH}_4)_2\text{MoO}_2\text{S}_2$ and its UV-Vis optical absorption spectrum, the schematics of the cell used for chronoamperometric measurements, the evolution of the coulombic efficiencies of Li-S cells with various additives, EIS curves of pristine Li-S with(out) $\text{MoX}_2\text{S}_2^{2-}$ (X: O, S) additives, SEM of the

bucky paper carbon host, crystal data and structure refinement details, fractional atomic coordinates and isotropic displacement parameters, anisotropic displacement parameters, and selected bond lengths for $[(\text{CH}_3)_4\text{N}]_2[(\eta\text{-S}_2)\text{Mo}_2\text{O}_2(\mu\text{-S})_2(\eta\text{-S}_4)]\cdot\text{CH}_3\text{CN}$, and EIS refined parameters. The cif for $[(\text{CH}_3)_4\text{N}]_2[(\eta\text{-S}_2)\text{Mo}_2\text{O}_2(\mu\text{-S})_2(\eta\text{-S}_4)]\cdot\text{CH}_3\text{CN}$ is also provided in the supporting information.

ACKNOWLEDGMENTS

This work was supported by the National Science Foundation, Division of Chemical, Bioengineering, Environmental, and Transport Systems, under award number 2011415 and the Welch Foundation grant F-1254.

REFERENCES

- (1) Manthiram, A.; Fu, Y.; Chung, S.-H.; Zu, C.; Su, Y.-S. Rechargeable Lithium–Sulfur Batteries. *Chem. Rev.* **2014**, *114* (23), 11751–11787. <https://doi.org/10.1021/cr500062v>.
- (2) Chung, S.-H.; Chang, C.-H.; Manthiram, A. Progress on the Critical Parameters for Lithium–Sulfur Batteries to Be Practically Viable. *Adv. Funct. Mater.* **2018**, *28* (28), 1801188. <https://doi.org/10.1002/adfm.201801188>.
- (3) Pang, Q.; Liang, X.; Kwok, C. Y.; Nazar, L. F. Advances in Lithium–Sulfur Batteries Based on Multifunctional Cathodes and Electrolytes. *Nat. Energy* **2016**, *1* (9), 1–11. <https://doi.org/10.1038/nenergy.2016.132>.
- (4) Li, G.; Chen, Z.; Lu, J. Lithium-Sulfur Batteries for Commercial Applications. *Chem* **2018**, *4* (1), 3–7. <https://doi.org/10.1016/j.chempr.2017.12.012>.
- (5) Yu, X.; Manthiram, A. A Progress Report on Metal–Sulfur Batteries. *Adv. Funct. Mater.* **2020**, *30* (39), 2004084. <https://doi.org/10.1002/adfm.202004084>.
- (6) Bruce, P. G.; Freunberger, S. A.; Hardwick, L. J.; Tarascon, J.-M. Li–O₂ and Li–S Batteries with High Energy Storage. *Nat. Mater.* **2012**, *11* (1), 19–29. <https://doi.org/10.1038/nmat3191>.
- (7) Zhao, M.; Li, B.-Q.; Zhang, X.-Q.; Huang, J.-Q.; Zhang, Q. A Perspective toward Practical Lithium–Sulfur Batteries. *ACS Cent. Sci.* **2020**, *6* (7), 1095–1104. <https://doi.org/10.1021/acscentsci.0c00449>.

- (8) Chung, S.-H.; Manthiram, A. Current Status and Future Prospects of Metal–Sulfur Batteries. *Adv. Mater.* **2019**, *31* (27), 1901125. <https://doi.org/10.1002/adma.201901125>.
- (9) Cheng, X.-B.; Yan, C.; Huang, J.-Q.; Li, P.; Zhu, L.; Zhao, L.; Zhang, Y.; Zhu, W.; Yang, S.-T.; Zhang, Q. The Gap between Long Lifespan Li-S Coin and Pouch Cells: The Importance of Lithium Metal Anode Protection. *Energy Storage Mater.* **2017**, *6*, 18–25. <https://doi.org/10.1016/j.ensm.2016.09.003>.
- (10) Yan, C.; Zhang, X.-Q.; Huang, J.-Q.; Liu, Q.; Zhang, Q. Lithium-Anode Protection in Lithium–Sulfur Batteries. *Trends Chem.* **2019**, *1* (7), 693–704. <https://doi.org/10.1016/j.trechm.2019.06.007>.
- (11) Luo, L.; Chung, S.-H.; Yaghoobnejad Asl, H.; Manthiram, A. Long-Life Lithium–Sulfur Batteries with a Bifunctional Cathode Substrate Configured with Boron Carbide Nanowires. *Adv. Mater.* **2018**, *30* (39), 1804149. <https://doi.org/10.1002/adma.201804149>.
- (12) He, J.; Bhargav, A.; Manthiram, A. Molybdenum Boride as an Efficient Catalyst for Polysulfide Redox to Enable High-Energy-Density Lithium–Sulfur Batteries. *Adv. Mater.* **2020**, *32* (40), 2004741. <https://doi.org/10.1002/adma.202004741>.
- (13) He, J.; Manthiram, A. 3D CoSe@C Aerogel as a Host for Dendrite-Free Lithium-Metal Anode and Efficient Sulfur Cathode in Li–S Full Cells. *Adv. Energy Mater.* **2020**, *10* (41), 2002654. <https://doi.org/10.1002/aenm.202002654>.
- (14) Bhargav, A.; He, J.; Gupta, A.; Manthiram, A. Lithium-Sulfur Batteries: Attaining the Critical Metrics. *Joule* **2020**, *4* (2), 285–291. <https://doi.org/10.1016/j.joule.2020.01.001>.
- (15) Eady, R. R. Structure–Function Relationships of Alternative Nitrogenases. *Chem. Rev.* **1996**, *96* (7), 3013–3030. <https://doi.org/10.1021/cr950057h>.
- (16) Seefeldt, L. C.; Hoffman, B. M.; Dean, D. R. Mechanism of Mo-Dependent Nitrogenase. *Annu. Rev. Biochem.* **2009**, *78* (1), 701–722. <https://doi.org/10.1146/annurev.biochem.78.070907.103812>.
- (17) Schindelin, H.; Kisker, C.; Hilton, J.; Rajagopalan, K. V.; Rees, D. C. Crystal Structure of DMSO Reductase: Redox-Linked Changes in Molybdopterin Coordination. *Science* **1996**, *272* (5268), 1615–1621. <https://doi.org/10.1126/science.272.5268.1615>.
- (18) Mom, R. V.; Louwen, J. N.; Frenken, J. W. M.; Groot, I. M. N. In Situ Observations of an Active MoS₂ Model Hydrodesulfurization Catalyst. *Nat. Commun.* **2019**, *10* (1), 2546. <https://doi.org/10.1038/s41467-019-10526-0>.
- (19) McAllister, J.; Bandeira, N. A. G.; McGlynn, J. C.; Ganin, A. Y.; Song, Y. F.; Bo, C.; Miras, H. N. Tuning and Mechanistic Insights of Metal Chalcogenide Molecular Catalysts for the Hydrogen-Evolution Reaction. *Nat. Commun.* **2019**, *10* (1), 1–10. <https://www.nature.com/articles/s41467-018-08208-4>.
- (20) McDonald, J. W.; Friesen, G. D.; Rosenhein, L. D.; Newton, W. E. Syntheses and Characterization of Ammonium and Tetraalkylammonium Thiomolybdates and Thiotungstates. *Inorganica Chim. Acta* **1983**, *72* (C), 205–210. [https://doi.org/10.1016/S0020-1693\(00\)81720-X](https://doi.org/10.1016/S0020-1693(00)81720-X).
- (21) Hadjikyriacou, A. I.; Coucouvanis, D. New Members of the [Mo₂(S)_n(S₂)_{6-n}]²⁻ Series. Synthesis, Structural Characterization, and Properties of the [Mo₂S₉]²⁻, [Mo₂S₇]²⁻, and [Mo₂S₆]²⁻ Thio Anions. *Inorg. Chem.* **1987**, *26* (15), 2400–2408. <https://doi.org/10.1021/ic00262a014>.
- (22) Hadjikyriacou, A. I.; Coucouvanis, D.; Enemark, J. H.; Backes-Dahmann, G. Tetraphenylphosphonium Salts of [Mo₂(S) N (S₂)_{6-N}]²⁻ Thioanions and Derivatives. In

- Inorganic Syntheses*; John Wiley & Sons, Ltd, 1990; pp 39–47.
<https://doi.org/10.1002/9780470132586.ch8>.
- (23) Müller, A.; Krickemeyer, E.; Hadjikyriacou, A.; Coucouvanis, D. Molybdenum-Sulfur Clusters. In *Inorganic Syntheses*; John Wiley & Sons, Ltd, 1990; pp 47–51.
<https://doi.org/10.1002/9780470132586.ch9>.
- (24) Clegg, W.; Christou, G.; Garner, C. D.; Sheldrick, G. M. [Mo₂S₁₀]²⁻, a Complex with Terminal Sulfido, Bridging Sulfido, Persulfido, and Tetrasulfido Groups. *Inorg. Chem.* **1981**, *20* (5), 1562–1566. <https://doi.org/10.1021/ic50219a045>.
- (25) Draganjac, M.; Simhon, E.; Chan, L. T.; Kanatzidis, M.; Baenziger, N. C.; Coucouvanis, D. Synthesis, Interconversions, and Structural Characterization of the Molybdenum Sulfide Anions, [(S₄)₂MoS]²⁻, [(S₄)₂MoO]²⁻, (Mo₂S₁₀)²⁻ and (Mo₂S₁₂)²⁻. *Inorg. Chem.* **1982**, *21* (9), 3321–3332. <https://doi.org/10.1021/ic00139a014>.
- (26) Pan, W. H.; Harmer, M. A.; Halbert, T. R.; Stiefel, E. I. Induced Internal Redox Processes in Molybdenum-Sulfur Chemistry: Conversion of Tetrathiomolybdate(2-) Ion to Octathiodimolybdate(2-) Ion by Organic Disulfides. *J. Am. Chem. Soc.* **1984**, *106* (2), 459–460. <https://doi.org/10.1021/ja00314a054>.
- (27) Cohen, S. A.; Stiefel, E. I. Dinuclear Tungsten(V) and Molybdenum(V) Compounds Containing M₂S₂(.Mu.-S)₂₂₊ Cores. Synthesis and Reactivity of [N(C₂H₅)₄]₂M₂S₁₂ (M = W or Mo) and the Crystal Structure of [N(C₂H₅)₄]₂W₂S₂(.Mu.-S)₂(S₄)₂. *Inorg. Chem.* **1985**, *24* (26), 4657–4662. <https://doi.org/10.1021/ic00220a046>.
- (28) Gupta, A.; Bhargava, A.; Manthiram, A. Highly Solvating Electrolytes for Lithium–Sulfur Batteries. *Adv. Energy Mater.* **2019**, *9* (6), 1803096.
<https://doi.org/10.1002/aenm.201803096>.
- (29) Dessapt, R.; Simonnet-Jégat, C.; Mallard, A.; Lavanant, H.; Marrot, J.; Sécheresse, F. Novel Mo(V)-Dithiolene Compounds: Characterization of Nonsymmetric Dithiolene Complexes by Electrospray Ionization Mass Spectrometry. *Inorg. Chem.* **2003**, *42* (20), 6425–6431. <https://doi.org/10.1021/ic0342907>.
- (30) Rittner, W.; Müller, A.; Neumann, A.; Bätcher, W.; Sharma, R. C. Generation of the Triangulo-Group MOV-η-S₂ in the “Condensation” of [MoVIO₂S₂]₂ to [MoO₂S₂(S₂)₂]₂. **1979**. <https://doi.org/10.1002/ANIE.197905301>.
- (31) Steudel, R.; Chivers, T. The Role of Polysulfide Dianions and Radical Anions in the Chemical, Physical and Biological Sciences, Including Sulfur-Based Batteries. *Chem. Soc. Rev.* **2019**, *48* (12), 3279–3319. <https://doi.org/10.1039/C8CS00826D>.
- (32) Wujcik, K. H.; Pascal, T. A.; Pemmaraju, C. D.; Devaux, D.; Stolte, W. C.; Balsara, N. P.; Prendergast, D. Characterization of Polysulfide Radicals Present in an Ether-Based Electrolyte of a Lithium–Sulfur Battery During Initial Discharge Using In Situ X-Ray Absorption Spectroscopy Experiments and First-Principles Calculations. *Adv. Energy Mater.* **2015**, *5* (16), 1500285. <https://doi.org/10.1002/aenm.201500285>.
- (33) Zhang, G.; Yi, H.; Chen, H.; Bian, C.; Liu, C.; Lei, A. Trisulfur Radical Anion as the Key Intermediate for the Synthesis of Thiophene via the Interaction between Elemental Sulfur and NaOtBu. *Org. Lett.* **2014**, *16* (23), 6156–6159. <https://doi.org/10.1021/ol503015b>.
- (34) Gu, Z.-Y.; Cao, J.-J.; Wang, S.-Y.; Ji, S.-J. The Involvement of the Trisulfur Radical Anion in Electron-Catalyzed Sulfur Insertion Reactions: Facile Synthesis of Benzothiazine Derivatives under Transition Metal-Free Conditions. *Chem. Sci.* **2016**, *7* (7), 4067–4072. <https://doi.org/10.1039/C6SC00240D>.

- (35) Nanda, S.; Bhargav, A.; Jiang, Z.; Zhao, X.; Liu, Y.; Manthiram, A. Implications of in Situ Chalcogen Substitutions in Polysulfides for Rechargeable Batteries. *Energy Environ. Sci.* **2021**, *14* (10), 5423–5432. <https://doi.org/10.1039/D1EE01113H>.
- (36) Nanda, S.; Bhargav, A.; Manthiram, A. Anode-Free, Lean-Electrolyte Lithium-Sulfur Batteries Enabled by Tellurium-Stabilized Lithium Deposition. *Joule* **2020**, *4* (5), 1121–1135. <https://doi.org/10.1016/j.joule.2020.03.020>.
- (37) Giannozzi, P.; Baroni, S.; Bonini, N.; Calandra, M.; Car, R.; Cavazzoni, C.; Ceresoli, D.; Chiarotti, G. L.; Cococcioni, M.; Dabo, I.; Corso, A. D.; Gironcoli, S. de; Fabris, S.; Fratesi, G.; Gebauer, R.; Gerstmann, U.; Gougoussis, C.; Kokalj, A.; Lazzeri, M.; Martin-Samos, L.; Marzari, N.; Mauri, F.; Mazzarello, R.; Paolini, S.; Pasquarello, A.; Paulatto, L.; Sbraccia, C.; Scandolo, S.; Sclauzero, G.; Seitsonen, A. P.; Smogunov, A.; Umari, P.; Wentzcovitch, R. M. QUANTUM ESPRESSO: A Modular and Open-Source Software Project for Quantum Simulations of Materials. *J. Phys. Condens. Matter* **2009**, *21* (39), 395502. <https://doi.org/10.1088/0953-8984/21/39/395502>.
- (38) Perdew, J. P.; Ernzerhof, M.; Burke, K. Generalized Gradient Approximation Made Simple. *Phys. Rev. Lett.* **1996**, *77*, 3865–3868. <https://doi.org/10.1103/PhysRevLett.77.3865>.
- (39) Martyna, G. J.; Tuckerman, M. E. A Reciprocal Space Based Method for Treating Long Range Interactions in Ab Initio and Force-Field-Based Calculations in Clusters. *J. Chem. Phys.* **1999**. <https://doi.org/10.1063/1.477923>.
- (40) Andreussi, O.; Dabo, I.; Marzari, N. Revised Self-Consistent Continuum Solvation in Electronic-Structure Calculations. *J. Chem. Phys.* **2012**, *136* (6), 064102. <https://doi.org/10.1063/1.3676407>.